

## Fourier transform-based design of a patterned piezoelectric energy harvester integrated with an elastoacoustic mirror

M. Carrara,<sup>1</sup> J. A. Kulpe,<sup>2</sup> S. Leadenham,<sup>2</sup> M. J. Leamy,<sup>2</sup> and A. Erturk<sup>2,a)</sup>

<sup>1</sup>*D. Guggenheim School of Aerospace Engineering, Georgia Institute of Technology, Atlanta, Georgia 30332, USA*

<sup>2</sup>*G. W. Woodruff School of Mechanical Engineering, Georgia Institute of Technology, Atlanta, Georgia 30332, USA*

(Received 27 August 2014; accepted 23 December 2014; published online 8 January 2015)

We explore efficient transformation of structure-borne propagating waves into low-power electricity using patterned polymer piezoelectrics integrated with an elastoacoustic mirror configuration. Fourier transform-based spatial optimization of a piezoelectric energy harvester domain weakly coupled to a thin plate housing a continuous elliptical elastoacoustic mirror is presented. Computational modeling and experimental testing are employed to quantify performance enhancement in power generation using the presented approach. Excellent agreement is observed between numerical simulations and experimental measurements. Specifically, dramatic enhancement of the harvested power output is reported by patterning the electrodes of a rectangular polyvinylidene fluoride piezoelectric energy harvester in the elliptical mirror domain. © 2015 AIP Publishing LLC. [<http://dx.doi.org/10.1063/1.4905509>]

Over the past decade, the harvesting of waste mechanical energy for low-power electricity generation has been heavily researched.<sup>1,2</sup> The ultimate goal in energy harvesting research is to enable self-powered wireless electronic components such as integrated sensor nodes used for structural health monitoring and assessment. This would enable the elimination of battery replacement and disposal, thus lowering maintenance costs for on-board devices. The benefits from such a technology development would have a high impact in various engineering systems, ranging from bridges<sup>3,4</sup> to unmanned aerial vehicle<sup>5</sup> applications. Although the harvesting of direct vibrational energy has been extensively studied through piezoelectric,<sup>6–9</sup> electrostatic,<sup>10,11</sup> electromagnetic,<sup>12,13</sup> and magnetostrictive<sup>14,15</sup> transduction mechanisms, as well as by electroactive polymers,<sup>16,17</sup> limited effort has been devoted to exploiting the energy of propagating waves in structures and fluids. Only a few research groups have addressed this area with the use of Helmholtz resonators,<sup>18</sup> sonic crystals,<sup>19</sup> and polarization-patterned piezoelectric solids<sup>20</sup> for structure-borne or air-borne wave energy harvesting. Others have investigated aeroelastic and hydroelastic phenomena for flow energy harvesting.<sup>21–24</sup> Recent studies showed that harvesting of propagating waves in structures can be enhanced through arrays of acoustic scatterers designed to focus, or properly localize, the associated acoustic energy. In particular, the effectiveness of elliptical<sup>25</sup> and parabolic<sup>26</sup> mirrors in focusing flexural waves, such as Lamb wave modes, has been demonstrated.

In this work, we propose a Fourier transform-based<sup>27</sup> (i.e., wavenumber-based<sup>28</sup>) design method to address the optimization of spatially distributed harvester (DH) configurations in order to enhance the energy extraction from incident waves by exploiting such mirrors. Harvester topology optimization has recently gained attention in the energy

harvesting community, and the importance of patterned polarization and electrode segmentation of the harvester has been discussed in vibration<sup>29–32</sup> and aeroelastic<sup>33</sup> energy harvesting cases. In the present work, we focus on topology optimization for the case of energy harvesting from propagating waves while exploiting an elastoacoustic mirror (EAM) for focusing. Additionally, unlike in the previous work by the authors,<sup>25,26</sup> a continuous mirror (instead of a discrete, stubbed one) is employed, while the harvester optimization process exploits a frequency-flattened wavenumber representation of the propagating wavefield inside the mirror domain. The goal is to develop a configuration that can maximize the electrical power output by proper wiring of the patterned electrodes targeting a specific frequency band.

In order to accurately model the propagation of transient elastic waves within the plate in the presence of a continuous EAM, the time-domain finite-element (FE) method is used. A FE model employing a symmetric boundary condition is implemented in COMSOL Multiphysics (Fig. 1(a)). The excitation input is a 5-cycle Hanning-windowed tone burst with center frequency of 50 kHz. The resulting root-mean-square (RMS) velocity field is presented in Fig. 1(b), where focusing of the waves is clearly visible. In particular, it can be noticed that the focal region is not confined to the geometrical focus of the EAM; instead, side lobes carrying significant energy levels are observed. This motivates studying patterned energy harvesters capable of extracting energy outside of the geometric focus.

To design an efficient and effective wave focusing mirror using a continuous elliptical strip, a parameter study is first performed to assess the height ( $H$ ) necessary to achieve focusing and minimize leakage. If  $H$  is too small, elastic waves see little impedance mismatch and hence scattering. Too large is detrimental to the system's weight, cost, and packaging. A series of transient simulations performed with  $H$  varying from 1 to 9 mm, while  $S$  (mirror thickness) is fixed

<sup>a)</sup>Author to whom correspondence should be addressed. Electronic mail: [alper.erturk@me.gatech.edu](mailto:alper.erturk@me.gatech.edu)

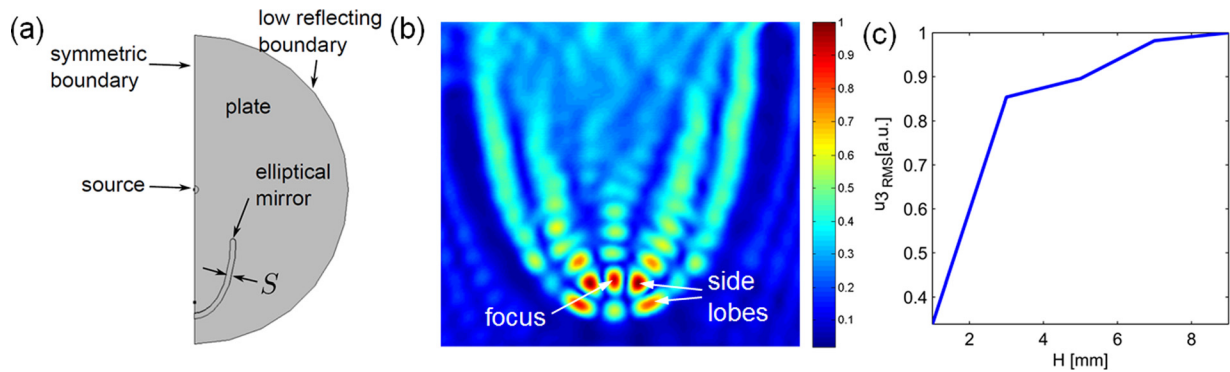


FIG. 1. (a) Schematic of the FE model for the continuous EAM configuration; (b) detail of the simulated RMS out-of-plane velocity distribution over the EAM domain, exhibiting focusing of the wave energy along with side lobes; and (c) RMS value of out-of-plane velocity at geometrical focus of the EAM with varying mirror height.

to 7 mm, is of particular interest for verifying energy leaking outside of the EAM. At each step, data post-processing enables calculation of the RMS of the out of plane velocity

$$u_{3_{RMS}}(\mathbf{x}) = \left( \int_0^t u_3(\mathbf{x}, t)^2 dt \right)^{\frac{1}{2}}, \quad (1)$$

where the RMS integration is done over the full time range of the FE simulation. The numerical results of  $u_{3_{RMS}}$  value at the geometrical focus point are displayed in Fig. 1(c). These indicate convergence in wave amplitude at focus as the mirror height  $H$  increases. Conversely, for  $H < 3$  mm, the focusing RMS-amplitude is weaker as the elliptical mirror leaks energy, thus failing to redirect it at its focus. Based on this parametric study, the mirror height is set  $H = 5$  mm hereafter, for negligible leakage and consistent focusing. The experimental EAM configuration corresponding to the simulated system is shown in Fig. 2(a) along with the patterned harvester domain. The patterned harvester is made from polyvinylidene fluoride (PVDF) of  $28 \mu\text{m}$  thickness (sheet type 1-1003702-7 from Measurement Specialties, Inc.), and therefore it is assumed to be weakly coupled to the system (the plate and EAM are aluminum), i.e., the presence of the PVDF harvester domain does not affect the wave field. The vacuum bonding

process (with high-shear-strength epoxy) employed to attach the PVDF to the aluminum plate is described elsewhere.<sup>34</sup>

In order to take advantage of this spatially confined energy spreading, we propose a wavenumber-based design procedure, which leads to optimally distributed electrode patterning able to further enhance energy extraction from the incoming waves. The first step is to perform a 3D Fourier transform of the full wave propagation field developing inside the EAM. Subsequently, an RMS average along the frequency domain is applied in order to better highlight the preferred propagation directions in the wavenumber domain. Note that the RMS along the frequency domain can, in principle, enable broadband energy harvesting capabilities. Next, a wavenumber amplitude threshold mask is applied and the DH is superimposed onto it. The resulting spatial shape has the following expression:

$$g(\mathbf{x}) = A(\mathbf{x}) \sum_{n=1}^N \cos(\boldsymbol{\kappa}_n^T \mathbf{x}), \quad (2)$$

where  $A(\mathbf{x})$  represents an arbitrary spatial extension of the DH *outer* shape (e.g., rectangular), while the term within the summation represents the *inner* shaping of the electrodes. In particular,  $\boldsymbol{\kappa}_n$  represents the  $n$ th wavenumber domain peak,  $\mathbf{x}$  represents the spatial domain, and  $N$  is the total number of wavenumber peaks given by the wavenumber amplitude masking procedure outlined before. The function  $g(\mathbf{x})$  indicates how the signal sensed at each point should be weighted. Such a configuration can hardly be realized experimentally, since it would require a continuously varying electrode distribution, which is impractical. For this reason, a second threshold is applied, and a three level discretization of the inner patterning is applied, leading to a two-electrode DH configuration (wiring 1 in Fig. 2(b)).

The performance of the continuous EAM and the DH configuration (wiring 1) are then investigated experimentally. In the experiments, the wave source is generated by a piezoelectric disk of 5 mm diameter and 0.4 mm thickness (STEMiNC Corp.) bonded to a 0.81 mm thick aluminum plate. The plate is excited by a sinusoidal burst (7 cycles) at selected frequencies, provided to the piezoelectric source by a function generator (Agilent 33220A) through a voltage amplifier (Trek Model PZD350). A Polytec PSV-400 scanning laser Vibrometer measures the resulting wavefield. Wavefield images and RMS distributions are obtained by

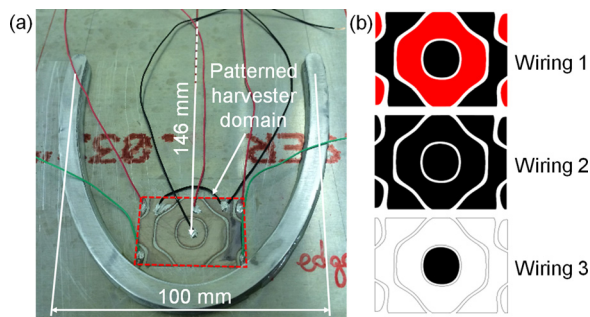


FIG. 2. (a) Experimental setup showing the continuous EAM and the patterned harvester (with the source-to-geometric focus distance and the minor axis length) and (b) electrode wiring configurations (same color areas are wired together). Wiring 1: positive (black) and negative (red) regions form the positive and negative terminals of the harvester, while the plate to which they are bonded acts as a shared ground. Wiring 2: positive and negative regions of the DH are connected in parallel to form the positive terminal, while the plate acts as negative terminal and ground. Wiring 3: single region of the DH overlapping the geometrical focus of the EAM forming the positive terminal, while the plate forms the negative terminal and ground.

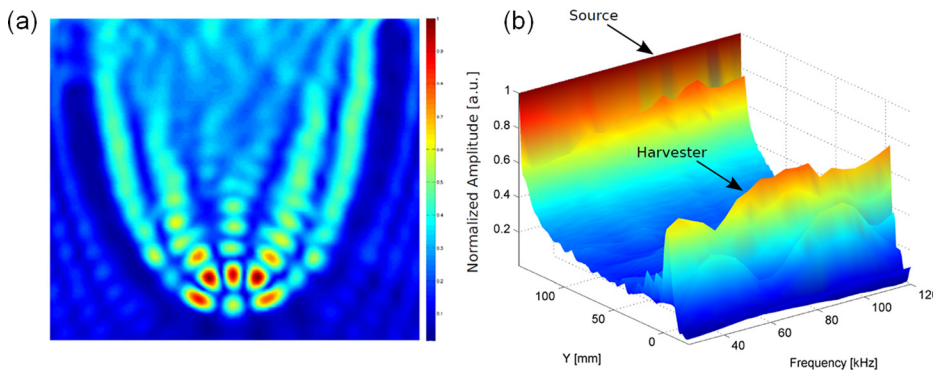


FIG. 3. Experimental results: (a) RMS velocity field for excitation at 50 kHz (the source region is excluded) for the continuous EAM configuration. Wave focusing at the location of the DH is clearly visible; (b) normalized RMS velocity field along the major axis of the EAM for the broad frequency range of 20–120 kHz showing the location of the source and of the harvester.

recording the out-of-plane plate response over a grid of points that overlaps the EAM region. Proper triggering of the laser measurements allows the reconstruction of the wavefield and the evaluation of the RMS through time integration of the recorded response. Fig. 3(a) displays experimentally obtained RMS distribution of the velocity field for excitation at 50 kHz and shows excellent agreement with the FE simulations (cf. Fig. 1(b)). Furthermore, focusing characteristics of the EAM are investigated by performing experiments in the 20–120 kHz range. At each frequency, the response of the plate is measured along the centerline of the EAM, i.e., the major axis of the elliptical layout. The results are summarized in Fig. 3(b), which shows the variation of the normalized wave amplitude along the centerline as a function of the excitation frequency. Amplitude normalization is conducted with respect to the amplitude at the excitation location, in order to compensate for the frequency-dependent coupling between the actuator (source) PZT disk and the host plate.<sup>25</sup> The results clearly illustrate how the velocity field is amplified by the EAM at the focal point of the ellipse in a broadband sense.

With the wavefield experiments in place, experiments are conducted to verify the improved power generation capabilities for the DH (wiring 1 in Fig. 2(b)) versus the two alternative wiring configurations (wiring 2 and wiring 3 in Fig. 2(b)). The energy harvesting experiments for all three configurations consist of resistor sweep tests, wherein the opposite terminals are shunted by range of load resistances (IET Labs, Inc., decade resistance substitution box). The voltage across the resistor is measured with an oscilloscope (Tektronix TDS2024) and used to calculate the power generated by the harvester. The excitation consists of 7-cycle sine bursts at 30, 40, 50, 60, and 70 kHz, similar to the previous experiments. Fig. 4 displays

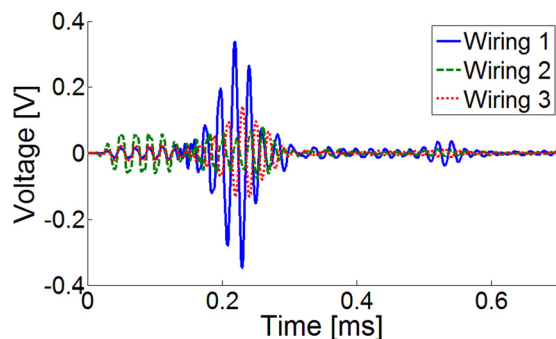


FIG. 4. Representative voltage responses of different wiring configurations to a 7-cycle 50 kHz sine burst excitation (for a 100 kΩ load resistance).

representative voltage response waveforms for the DH and the two alternative wiring configurations for 100 kΩ load resistance (quasi open-circuit condition).

In the voltage response of the harvester (e.g., Fig. 4), two undesirable signal artifacts are present due to experimental limitations. Because the excitation is provided by a piezoelectric disk, which shares the host plate as an electrical terminal with the harvester, the electrical excitation provided to the system is seen in the harvester voltage response in the first 0.15 ms. After approximately 0.5 ms, a response due to reflections from the plate edge are also observed. Evaluating the harvester performance based on the RMS of the response voltage to the incident wave, occurring roughly between 0.15 and 0.3 ms, eliminates these artifacts from subsequent analysis. Fig. 5 illustrates the RMS response voltage, current, and power generation characteristics of the three wiring configurations when excited by the 50 kHz sine burst used in the patterning design.

When excited by the 50 kHz sine burst used in the wavefield modeling and harvester pattern design, the patterned electrode design (wiring 1) clearly outperforms the other two wiring configurations. At this frequency level, wiring 1 generates a peak power 4.3 times greater than wiring 2 and 7.3 times greater than wiring 3. Optimal power output occurs for the three wiring configurations at different load resistance values due to their different capacitance values. Experimental optimal load resistances and peak power output for the three wiring configurations at various sine burst center frequencies are summarized in Table I.

The patterned harvester (wiring 1) produces the most power when excited by the 40 kHz 7-cycle sine burst rather than the 50 kHz sine burst around which it was designed. This may be due to manufacturing imperfections. Wiring 1

TABLE I. Performance comparison of wiring 1, 2, and 3 at various excitation center frequencies. For each, the optimal average power generation for each frequency,  $P_{\text{opt}}$ , is given along with the corresponding matched load resistance value,  $R_{\text{opt}}$ .

Frequency (kHz)	Wiring 1		Wiring 2		Wiring 3	
	$R_{\text{opt}}$ (kΩ)	$P_{\text{opt}}$ (μW)	$R_{\text{opt}}$ (kΩ)	$P_{\text{opt}}$ (μW)	$R_{\text{opt}}$ (kΩ)	$P_{\text{opt}}$ (μW)
30	25	1.143	6.3	0.069	40	0.139
40	15	1.644	6.3	0.074	25	0.091
50	15	0.637	4	0.149	15	0.087
60	10	0.276	4	0.293	15	0.057
70	10	0.307	4	0.808	15	0.019

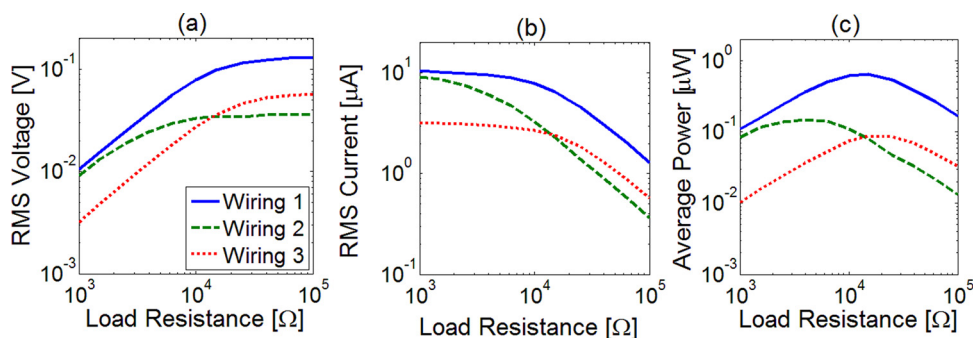


FIG. 5. Root-mean-square (a) voltage, (b) current, and (c) average power performance curves for wiring 1, wiring 2, and wiring 3 in response to a 7-cycle 50 kHz sine burst excitation for a set of resistive loads varying from 1 k $\Omega$  to 100 k $\Omega$ .

and wiring 3 both show the same decreasing trend of peak power output, while wiring 2 shows a rise in power output with increased frequency. The patterned harvester (wiring 1) outperforms wiring 3 at all frequencies and outperforms wiring 2 at frequencies below 60 kHz. Therefore, the patterned piezoelectric energy harvester integrated with an elastoacoustic mirror results in enhanced structure-borne wave energy harvesting and robustness around the center frequency used in pattern design. Further electrode segmentation would be required to enhance the frequency bandwidth of the patterned configuration for the maximum power output over a wide range of frequencies. The electrical circuit can also be improved for complex load impedance matching to boost the power output.<sup>35</sup>

Overall, an experimentally validated procedure for design of spatially distributed piezoelectric energy harvesters integrated with elastoacoustic mirrors has been presented for efficient electrical power generation from structure-borne propagating waves. Accurate FE modeling of the focusing mirror leads to the design of an optimally distributed harvester. The effectiveness of the proposed configuration is verified experimentally, where significant improvement of power output over two comparison configurations have been reported. While the focus point offers the largest power extraction per harvester area in the local sense, the total power output can be enhanced significantly by collecting the electric charge developed in the neighboring lobes as well. The procedure can also be used for a parabolic mirror<sup>26</sup> in plane wave energy harvesting.

This work was supported by the National Science Foundation under Grant No. CMMI-1333978.

<sup>1</sup>K. Cook-Chennault, N. Thambi, and A. Sastry, *Smart Mater. Struct.* **17**(4), 043001 (2008).

<sup>2</sup>N. S. Hudak and G. G. Amatucci, *J. Appl. Phys.* **103**(10), 101301 (2008).

<sup>3</sup>S. F. Ali, M. Friswell, and S. Adhikari, *J. Intell. Mater. Syst. Struct.* **22**(16), 1929–1938 (2011).

<sup>4</sup>A. Erturk, *J. Intell. Mater. Syst. Struct.* **22**(17), 1959–1973 (2011).

<sup>5</sup>S. R. Anton, A. Erturk, and D. J. Inman, *J. Airc.* **49**(1), 292–301 (2012).

<sup>6</sup>A. Erturk, J. Hoffmann, and D. Inman, *Appl. Phys. Lett.* **94**(25), 254102 (2009).

<sup>7</sup>A. Erturk and D. J. Inman, *Piezoelectric Energy Harvesting* (Wiley, Chichester, UK, 2011).

<sup>8</sup>S. C. Stanton, C. C. McGehee, and B. P. Mann, *Appl. Phys. Lett.* **95**(17), 174103 (2009).

<sup>9</sup>S. C. Stanton, A. Erturk, B. P. Mann, E. H. Dowell, and D. J. Inman, *J. Intell. Mater. Syst. Struct.* **23**(2), 183–199 (2012).

<sup>10</sup>P. D. Mitcheson, P. Miao, B. H. Stark, E. Yeatman, A. Holmes, and T. Green, *Sens. Actuators, A* **115**(2), 523–529 (2004).

<sup>11</sup>S. Roundy, P. K. Wright, and J. M. Rabaey, *Energy Scavenging for Wireless Sensor Networks with Special Focus on Vibrations* (Springer, 2004).

<sup>12</sup>D. P. Arnold, *IEEE Trans. Magn.* **43**(11), 3940–3951 (2007).

<sup>13</sup>P. Glynne-Jones, M. Tudor, S. Beeby, and N. White, *Sens. Actuators, A* **110**(1), 344–349 (2004).

<sup>14</sup>L. Wang and F. Yuan, *Smart Mater. Struct.* **17**(4), 045009 (2008).

<sup>15</sup>X. Xing, J. Lou, G. Yang, O. Obi, C. Driscoll, and N. Sun, *Appl. Phys. Lett.* **95**(13), 134103 (2009).

<sup>16</sup>M. Aureli, C. Prince, M. Porfiri, and S. D. Peterson, *Smart Mater. Struct.* **19**(1), 015003 (2010).

<sup>17</sup>S. J. A. Koh, X. Zhao, and Z. Suo, *Appl. Phys. Lett.* **94**(26), 262902 (2009).

<sup>18</sup>S. B. Horowitz, M. Sheplak, L. N. Cattafesta III, and T. Nishida, *J. Micromech. Microeng.* **16**(9), S174 (2006).

<sup>19</sup>L.-Y. Wu, L.-W. Chen, and C.-M. Liu, *Appl. Phys. Lett.* **95**(1), 013506 (2009).

<sup>20</sup>C. J. Rupp, M. L. Dunn, and K. Maute, *Appl. Phys. Lett.* **96**(11), 111902 (2010).

<sup>21</sup>A. Erturk, W. Vieira, C. De Marqui, Jr., and D. Inman, *Appl. Phys. Lett.* **96**(18), 184103 (2010).

<sup>22</sup>A. Giacomello and M. Porfiri, *J. Appl. Phys.* **109**(8), 084903–084910 (2011).

<sup>23</sup>J. Dias, C. De Marqui, Jr., and A. Erturk, *Appl. Phys. Lett.* **102**(4), 044101 (2013).

<sup>24</sup>A. Erturk and G. Delporte, *Smart Mater. Struct.* **20**(12), 125013 (2011).

<sup>25</sup>M. Carrara, M. Cacan, M. Leamy, M. Ruzzene, and A. Erturk, *Appl. Phys. Lett.* **100**(20), 204105 (2012).

<sup>26</sup>M. Carrara, M. Cacan, J. Toussaint, M. Leamy, M. Ruzzene, and A. Erturk, *Smart Mater. Struct.* **22**(6), 065004 (2013).

<sup>27</sup>K. F. Graff, *Wave Motion in Elastic Solids* (Courier Dover Publications, 1975).

<sup>28</sup>F. J. Fahy and P. Gardonio, *Sound and Structural Vibration: Radiation, Transmission and Response* (Academic Press, 2007).

<sup>29</sup>S. Kim, W. W. Clark, and Q.-M. Wang, *J. Intell. Mater. Syst. Struct.* **16**(10), 847–854 (2005).

<sup>30</sup>S. Kim, W. W. Clark, and Q.-M. Wang, *J. Intell. Mater. Syst. Struct.* **16**(10), 855–863 (2005).

<sup>31</sup>C. J. Rupp, A. Evgrafov, K. Maute, and M. L. Dunn, *J. Intell. Mater. Syst. Struct.* **20**(16), 1923–1939 (2009).

<sup>32</sup>M. I. Friswell and S. Adhikari, *J. Appl. Phys.* **108**(1), 014901 (2010).

<sup>33</sup>C. De Marqui, A. Erturk, and D. J. Inman, *J. Intell. Mater. Syst. Struct.* **21**(10), 983–993 (2010).

<sup>34</sup>S. Anton, A. Erturk, and D. Inman, *Smart Mater. Struct.* **19**(11), 115021 (2010).

<sup>35</sup>N. Elvin and A. Erturk, *Advances in Energy Harvesting Methods* (Springer, 2013).